

The Southeast Pacific Warm Band and Double ITCZ

HIROHIKO MASUNAGA

Hydrospheric Atmospheric Research Center, Nagoya University, Nagoya, Japan

TRISTAN S. L'ECUYER

Department of Atmospheric Science, Colorado State University, Fort Collins, Colorado

(Manuscript received 9 March 2009, in final form 11 August 2009)

ABSTRACT

The east Pacific double intertropical convergence zone (ITCZ) in austral fall is investigated with particular focus on the growing processes of its Southern Hemisphere branch. Satellite measurements from the Tropical Rainfall Measuring Mission (TRMM) and Quick Scatterometer (QuikSCAT) are analyzed to derive 8-yr climatology from 2000 to 2007. The earliest sign of the south ITCZ emerges in sea surface temperature (SST) by January, followed by the gradual development of surface convergence and water vapor. The shallow cumulus population starts growing to form the south ITCZ in February, a month earlier than vigorous deep convection is organized into the south ITCZ. The key factors that give rise to the initial SST enhancement or the southeast Pacific warm band are diagnosed by simple experiments. The experiments are designed to calculate SST, making use of an ocean mixed layer “model” forced by surface heat fluxes, all of which are derived from satellite observations. It is found that the shortwave flux absorbed into the ocean mixed layer is the primary driver of the southeast Pacific warm band. The warm band does not develop in boreal fall because the shortwave flux is seasonally so small that it is overwhelmed by other negative fluxes, including the latent heat and longwave fluxes. Clouds offset the net radiative flux by $10\text{--}15\text{ W m}^{-2}$, which is large enough for the warm band to develop in boreal fall if it were not for clouds reflecting shortwave radiation. Interannual variability of the double ITCZ is also discussed in brief.

1. Introduction

The intertropical convergence zone (ITCZ) over the east Pacific Ocean stays away from the equator by $5^{\circ}\text{--}10^{\circ}$ latitude, and is only to its north most time of the year. Many studies have investigated the possible origins of this off-equatorial preference and meridional asymmetry. A high sea surface temperature (SST) may be a factor that is instrumental for the geographical constraint on the ITCZ (Pike 1971), while other studies (Holton et al. 1971; Waliser and Somerville 1994, and references therein) attribute it to intrinsic atmospheric dynamics rather than to the presence of warm ocean beneath. The role of the underlying ocean, on the other hand, has been considered as being crucial for explaining the absence of the east Pacific ITCZ in the Southern Hemisphere.

SST remains low in the southeast Pacific, arguably as the result of an SST–wind–evaporation feedback (Xie and Philander 1994; Xie 1994), stratiform cloud decks (Mitchell and Wallace 1992; Philander et al. 1996), asymmetric coastline geometry (Philander et al. 1996), and other factors, including the seasonally varying solar forcing (Wang and Wang 1999).

A Southern Hemisphere branch of the ITCZ (hereafter “south ITCZ”) often emerges from March to April in the east Pacific, leading to a double ITCZ, together with its Northern Hemisphere counterpart (hereafter the north ITCZ), as documented from time to time (Hubert et al. 1969; Halpern and Hung 2001; Lietzke et al. 2001; Zhang 2001; Gu et al. 2005). Aside from Zhang (2001), who argued that SST could be a primary driver of the double ITCZ, the physical processes that account for how and why the south ITCZ develops have not been explored extensively. It is reasonable to expect that the meridionally symmetric insolation in this particular season should create symmetric warm oceanic bands straddling the equatorial cold tongue (Mitchell and Wallace

Corresponding author address: Hirohiko Masunaga, Hydrospheric Atmospheric Research Center, Nagoya University, F3-1(200) Furocho, Chikusa-ku, Nagoya 458-0015, Japan.
E-mail: masunaga@hyarc.nagoya-u.ac.jp

1992). This simple, intuitive hypothesis, however, is challenged by the fact that the south ITCZ is not observed at all in the other equinoctial season. We have no satisfactory explanation to date for what promotes the eastern Pacific ITCZ in austral fall *and* hampers it in boreal fall. Solving this problem would help us understand not only the transience of the south ITCZ, but potentially the stability of the north ITCZ as well.

In the present paper, the growing processes of the eastern Pacific south ITCZ are investigated from satellite observations. Data from a variety of satellite sensors, including a microwave radiometer, radar, and a scatterometer are utilized to analyze SST, columnar water vapor (CWV), the surface convergence field, and shallow and deep precipitating clouds (section 2). After the observed climatology is outlined in section 3, the satellite datasets are applied to evaluate the heat budget of the ocean mixed layer (section 4). Section 5 is devoted to discussing the factors that modulate mixed layer temperature variability. The present findings are concluded in section 6.

2. Data

It has been a decade since the Tropical Rainfall Measuring Mission (TRMM) satellite was launched in late 1997, so TRMM now provides a long observational record that is suitable for climatological analysis. Shallow and deep precipitating clouds can be distinguished using TRMM Precipitation Radar (PR) echo-top height and Visible and Infrared Scanner (VIRS) infrared brightness temperature (IR T_b ; Masunaga et al. 2005). Precipitating shallow cumulus is identified by rainfall with a PR echo-top height lower than 4 km. Cloud droplets are undetectable by the PR, and therefore nonprecipitating low clouds are not included in the shallow category defined here. Masunaga et al. (2005) originally define the shallow category with an additional constraint of IR $T_b > 265$ K, which is not imposed in this study in order to avoid missing shallow cumulus overcast by higher-level clouds. Towering cloud systems, or “deep stratiform” and “deep convective” systems combined together in the Masunaga et al. (2005) terminology, are delineated by PR echo tops that are higher than 4 km, collocated with IR T_b s colder than 245 K. This infrared threshold helps capture high cloud decks that would be left undetected by the PR alone, given that the PR sensitivity to ice condensates is marginal. The area coverage of shallow cumulus and towering clouds (hereafter shallow cumulus coverage and deep storm coverage, respectively) are used as the measure of convective activity for the individual cloud types.

SST and CWV are provided from the TRMM Microwave Imager (TMI) product created and distrib-

uted by the Remote Sensing Systems. The near-surface wind vector is provided from the Quick Scatterometer (QuikSCAT) SeaWinds level-3 daily gridded dataset. The wind vector field is used for computing surface convergence and surface wind stress. The satellite datasets are also applied to an ocean heat budget consideration described later (section 4). SST and CWV are used for evaluating latent heat flux. The QuikSCAT wind constrains the latent heat and ocean upwelling fluxes. Surface current data from the Ocean Surface Current Analysis–Real time (OSCAR; Bonjean and Lagerloef 2002) are employed to calculate the horizontal advection in the ocean mixed layer. The OSCAR current is calculated primarily from satellite altimeter and scatterometer products. Pentad time series of the filtered current velocity is linearly interpolated in time to a daily data sequence. The mixed layer depth is estimated with a variable density criterion using a dataset provided by de Boyer Montégut et al. (2004). The *World Ocean Atlas 2005* (WOA05; Locarnini et al. 2006) is adopted to estimate the temperature difference between the mixed layer and upwelling water from beneath. Surface radiative fluxes are provided by the Hydrologic Cycle and Earth Radiation Budget (HERB) product (L'Ecuyer and Stephens 2003; 2007; L'Ecuyer and McGarragh 2010), where the radiative fluxes are computed with the cloud and precipitation distribution observed from the TMI and VIRS instruments aboard the TRMM. Methodologies for estimating the surface heat fluxes are described in the appendix.

All satellite datasets are projected onto a common $1^\circ \times 1^\circ$ global grid. The daily and monthly climatologies of each parameter are then constructed from 8 yr of observation from 1 January 2000 to 31 December 2007. El Niño Southern Oscillation (ENSO) is relatively moderate in amplitude during this period, so that no effort is made to remove the ENSO components that might contaminate the climatological mean. Although the data are available across the entire globe (except for high latitudes out of reach from the TRMM satellite), the target area of the present work is limited to the tropical eastern Pacific, zonally bound between 150° and 75° or 85° W.

3. Climatology of the east Pacific double ITCZ

The observed characteristics of the east Pacific south ITCZ are first illustrated as analyzed from the 8-yr climatology. Figure 1 shows the monthly mean SST, deep storm coverage, and shallow cumulus coverage from December to March. Consistently observed throughout these months are the north ITCZ at 5° – 10° N and the northeastern edge of the South Pacific convergence zone (SPCZ), in the bottom-left corner of each panel. The

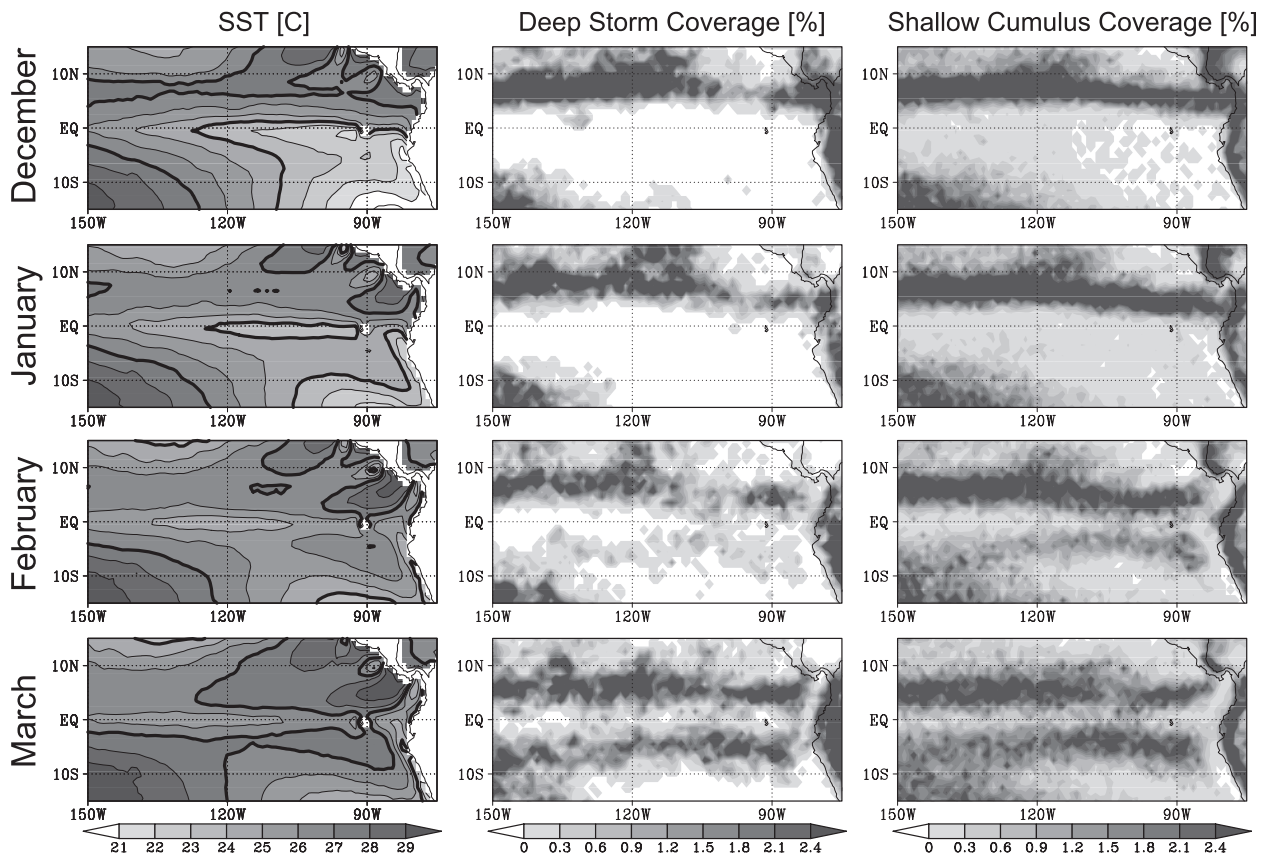


FIG. 1. Observed monthly climatologies of (left) SST ($^{\circ}\text{C}$), (middle) deep storm coverage (%), and (right) shallow cumulus coverage (%) for 15°S – 15°N , 150° – 75°W . SSTs of 24° and 27°C are highlighted by thick contours. (top to bottom) Different rows show subsequent months from December to March.

south ITCZ is absent in December, with the exception of a small area of warmer SST at 100°W . By January, this area has expanded into a band of warm water, hereafter called the southeast Pacific warm band (or simply the warm band), south of the equator, isolating the equatorial cold tongue from the cool water brought by the Humboldt Current. However, shallow and deep clouds do not show any corresponding pattern at this stage in the evolution of the south ITCZ. The warm band keeps growing through February, with a local SST maximum developing around 5°S , 90°W . At the same time, shallow cumulus begins to organize itself into the double ITCZ. The 90°W SST maximum extends westward and connects with the SPCZ in March, and the double ITCZ finally becomes evident in deep storm coverage as well as in shallow cumulus coverage.

Figure 2 illustrates the Hovmöller diagram, averaged over 12.5° – 2.5°S , of various parameters relevant to the south ITCZ. A steady sea surface warming is clearly observed from January through March in Fig. 2a, with the rate of SST increase highest around 90°W . The resultant “U”-like pattern is also evident in the surface

convergence calculated from QuikSCAT wind (Fig. 2f). The surface wind, which is divergent at the beginning, becomes convergent near 90°W at first, and then eventually across the entire tropical southeast Pacific. The Hovmöller diagram of CWV (Fig. 2d) implies a gradual but constant trend of moistening. The moistening results solely from local evaporation initially as long as surface convergence stays negative. The U pattern is again discernible in CWV, although it is not as well defined as that observed in SST and convergence. The rapid moistening near 90°W , once it starts to occur, implies that moisture convergence is now at work as the primary driver of moistening, because the latent heat flux monotonically declines eastward with no 90°W peak (Fig. 2e). The tropical southeast Pacific is increasingly populated by shallow cumulus in February and March, while it is not until March that deep storm coverage exhibits a systematic enhancement, as already seen in Fig. 1.

The parameters shown in Fig. 2 are projected together on daily time series in terms of the regional mean over the study area (12.5° – 2.5°S , 150° – 85°W) in Fig. 3. SST delineates a sinusoidal seasonal cycle, which is highest in

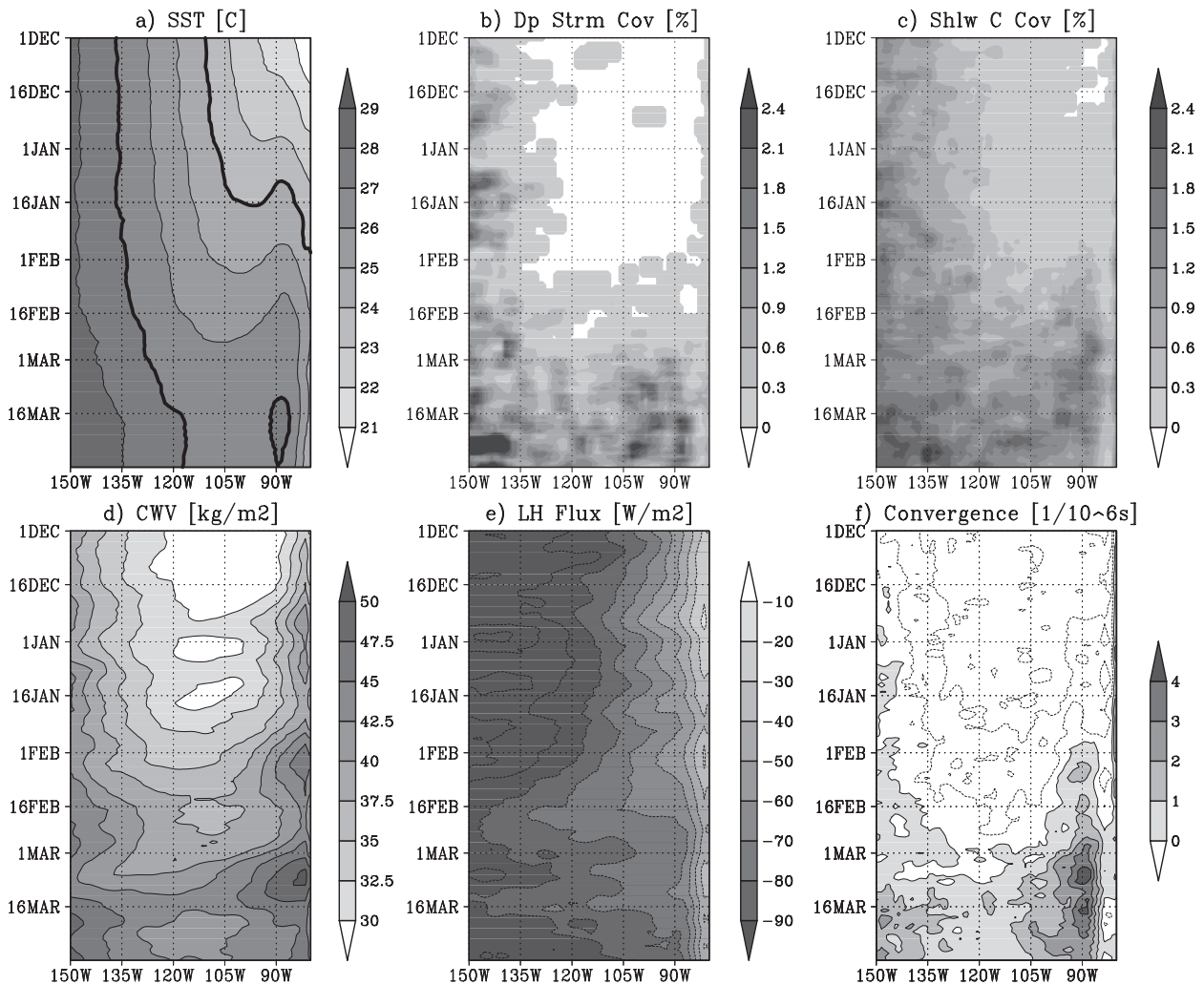


FIG. 2. Hovmöller diagram of observed daily climatologies meridionally averaged over 12.5°–2.5°S. (a) SST (°C) with 24° and 27°C contours highlighted, (b) deep storm coverage (%), and (c) shallow cumulus coverage (%). (d) CWV (kg m^{-2}), (e) latent heat flux (W m^{-2}), and (f) surface convergence (10^{-6} s^{-1}) with negative values (i.e., diverging areas) unshaded.

late March or early April. Shallow cumulus and deep storm coverage also vary seasonally but less sinusoidally than SST. The period of enhanced shallow cumulus population spans roughly a half-year from February to July. Shallow cumulus coverage stays at the background level of 0.3%–0.5% for the rest of the year. The period of enhanced population does not last as long as 2 months for deep clouds, and it shows a sharp rise and drop with the narrow maximum in between. The background level of deep storm coverage is nearly zero, indicating that deep convection is virtually absent, except when the south ITCZ is active. CWV and the surface convergence maximize in late March, in phase with SST. Interestingly, surface convergence shares the overall variability with shallow cumulus coverage, including the secondary peak in late May or early June. This resemblance may

suggest the presence of a dynamical link between surface convergence and the development of precipitation in shallow cumulus. The latent heat flux does not bear any apparent relevance to the south ITCZ in annual cycle.

The climatological characteristics of the double ITCZ are similar overall to that seen in past work (Halpern and Hung 2001; Lietzke et al. 2001; Zhang 2001; Gu et al. 2005). Figures 1–3, however, illustrate some notable aspects of the south ITCZ that have not been studied much before. First, a sign of the south ITCZ is visually traceable in SST even in austral summer, when the south ITCZ itself does not exist yet in terms of convergence field and precipitating cloud coverage. The southeast Pacific warm band steadily evolves for a few months to follow, with the local SST maximum around 90°W

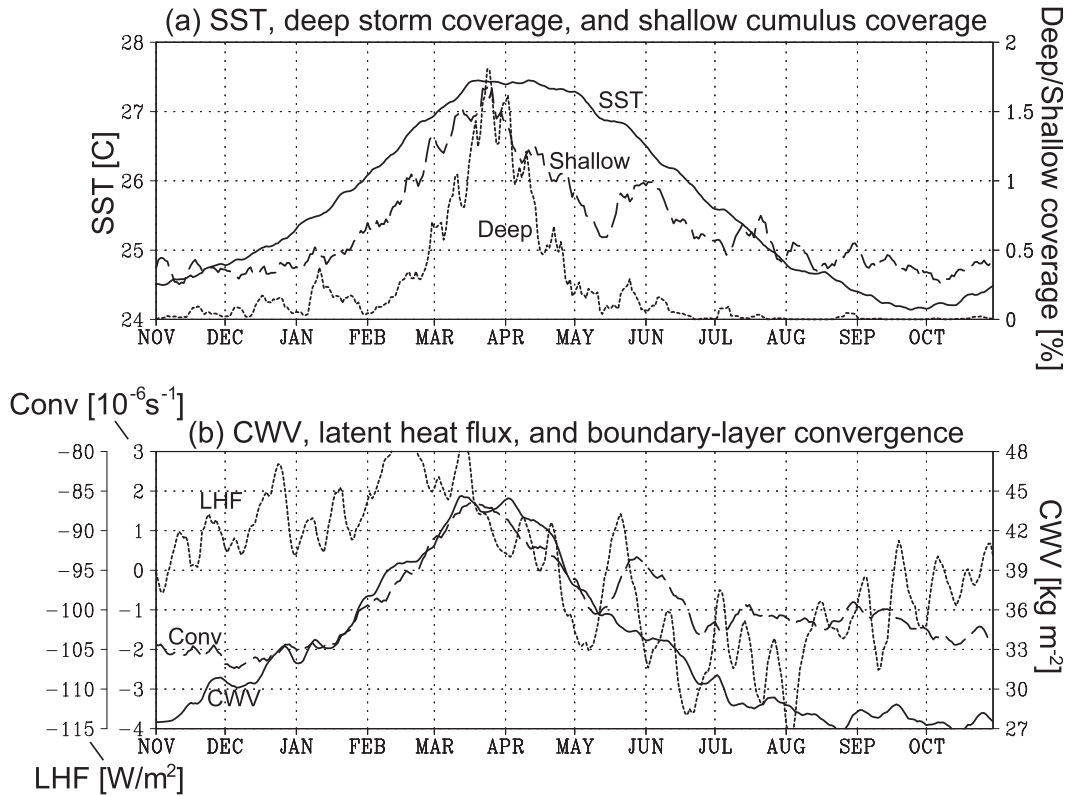


FIG. 3. Time series of observed daily climatologies regionally averaged over 12.5°–2.5°S, 150°–85°W. (a) SST (°C; solid), deep storm coverage(%; dotted), and shallow cumulus coverage(%; dashed). (b) CWV (kg m⁻²; solid), latent heat flux (LHF; W m⁻²; dotted), surface convergence (Conv; 10⁻⁶ s⁻¹; dashed).

leading the rest. Second, surface convergence, CWV, and shallow cumulus begin to form the south ITCZ pattern one after another, followed ultimately by the mature phase, which is marked with vigorous deep convection. As such, the south ITCZ does not abruptly manifest itself in austral fall, but instead undergoes a series of evolutionary stages initiated in the preceding summer.

The rest of this study is devoted to exploring the factors responsible for the observed SST variation in the tropical southeast Pacific, because the very initial sign of the south ITCZ seems to appear only in SST. To this end, simple experiments to diagnose the heat budget of the ocean mixed layer are carried out in the following section.

4. Diagnosis of SST controlling factors

In this section, the factors driving the southeast Pacific warm band are sought by considering the individual terms that contribute to the ocean heat budget. Results are presented after a short description of experimental setup.

a. Experimental setup

The heat budget of the ocean mixed layer may be written as

$$\rho_w H_{ml} C_{p,w} \frac{\partial T_s}{\partial t} = Q_{adv} + Q_{upw} + Q_{SW} + Q_{LW} + Q_{LH} + Q_{SH}, \quad (1)$$

where $\rho_w = 1030 \text{ kg m}^{-3}$ is the ocean water density, H_{ml} the mixed layer depth, $C_{p,w} = 4.0 \times 10^3 \text{ J kg}^{-1} \text{ K}^{-1}$ the specific heat of ocean water, T_s the SST, Q_{adv} the heat transport by horizontal advection within the mixed layer, Q_{upw} the heat transport by upwelling through the mixed layer bottom, Q_{SW} the shortwave energy flux absorbed into the mixed layer, Q_{LW} the net longwave flux at the surface, Q_{LH} the latent heat flux, and Q_{SH} the sensible heat flux. All Q terms are in watts per squared meter. The eddy diffusion of heat has been neglected. Each flux term in the RHS, except for Q_{SH} , is evaluated from satellite observations. See the appendix for details regarding the methodology for calculating each term in (1) with the exception of the sensible heat flux, which is

TABLE 1. Experimental setup. See text for more detail.

Run	Austral fall experiment (initiated on 1 Nov)	Boreal fall experiment (initiated on 1 Jul)
Control	All fluxes are varied daily	All fluxes are varied daily
LW ↓ fixed	F_{LW}^{\downarrow} is fixed at July	F_{LW}^{\downarrow} is fixed at January
LW ↑ fixed	F_{LW}^{\uparrow} is fixed at July	F_{LW}^{\uparrow} is fixed at January
SW fixed	Q_{SW} is fixed at July	Q_{SW} is fixed at January
LH fixed	Q_{LH} is fixed at July	Q_{LH} is fixed at January
ADV fixed	Q_{adv} is fixed at July	Q_{adv} is fixed at January
UpW fixed	Q_{upw} is fixed at July	Q_{upw} is fixed at January

not important for tropical oceans and is given a constant value of -10 W m^{-2} .

Two sets of simple experiments are performed with (1), forced by satellite-derived heat fluxes. The first is an “austral fall experiment,” where SST is initialized by the observed climatology of 1 November. Equation (1) is then integrated over time numerically at each $1^{\circ} \times 1^{\circ}$ grid point. In the control run, all of the fluxes are varied daily. Additional runs are conducted with one of the fluxes fixed at a “wrong” season, defined as the July climatology in this case, while the remaining terms are varied daily as done for the control. Each of the flux terms in (1) is “fixed” in turn, with the exception of Q_{SH} , and the upwelling and downwelling components of Q_{LW} , F_{LW}^{\uparrow} , and F_{LW}^{\downarrow} , are tested separately, resulting in six trials hereafter referred to as the LW↓ fixed, LW↑ fixed, SW fixed, LH fixed, ADV fixed, and UpW fixed runs, as listed in Table 1. The second experiment is a “boreal fall experiment,” which is identical to the austral fall experiment, except that the initial conditions are initiated to 1 July and the “wrong” month fluxes are fixed at their January climatologies.

These experiments are aimed at identifying the particular heat fluxes responsible for the southeast Pacific warm band. The key factors controlling the warm band must be distinctly seasonal, because the south ITCZ emerges only in austral fall and is suppressed for the remainder of the year. In the austral fall experiment, the flux terms critical for the development of the southeast Pacific warm band may be inferred by the runs that fail to reproduce the warm band under July conditions. These fluxes should, in turn, lead to a spurious warm band in the boreal fall experiment when forced by January conditions. The seasonal contrast in the individual flux terms between January and July will be examined in section 5a.

b. Results

The control run of the austral fall experiment is first compared with the observation. Figure 4 presents monthly mean SST for the first 3 months of the experiment. The experiment overestimates SST across the tropical southeast Pacific, except in the equatorial cold tongue where

SST is largely underestimated. Given the simplicity of its design, the current experiment is very limited in quantitative predictability and is by no means aimed at accurate forecasting of SST. In Fig. 4, nevertheless, the experiment proves to have some ability to reasonably reproduce the overall spatial pattern of SST. The estimated SST exhibits the southeast Pacific warm band as observed. This result encourages us to proceed further with the present analysis, provided the interpretation is restricted to a qualitative assessment of SST.

Different runs of the austral fall experiment are shown in the Hovmöller diagram in Fig. 5. The U pattern is roughly captured in the control run, although it is somewhat washed out near its eastern edge by the contamination of the strong cold tongue. The overall result is not altered when F_{LW}^{\downarrow} or F_{LW}^{\uparrow} is fixed at the July climatology (Figs. 5c,d). In contrast, replacing Q_{SW} with its July climatology results in a drastic change to SST (Fig. 5e) where the warm band is completely absent. The LH fixed run (Fig. 5f) yields little change to SST. The sea surface warming near the eastern end of the Pacific almost vanishes in the ADV and UpW fixed runs (Figs. 5g,h), destroying the U shape in the Hovmöller diagram. The advective and upwelling heat fluxes therefore have some impact on the southeast Pacific warm band, although the impact is not as dramatic as the absorbed shortwave flux.

Results from the boreal fall experiment are summarized in Fig. 6. Observed SST (Fig. 6a) shows no U pattern but only a monotonic eastward decline throughout the 6 months studied. This is as expected from the fact that the south ITCZ is absent in boreal fall. The control run (Fig. 6b) closely reproduces the observed SST for the first 3 months. The first sign of the southeast Pacific warm band appears in October in the control run a little too early relative to the observations. The result is insensitive to a change to the longwave flux (F_{LW}^{\downarrow} and F_{LW}^{\uparrow}) or to the latent heat flux as seen in Figs. 6c,d,f. It is again the absorbed shortwave flux that totally alters SST (Fig. 6e). The southeast Pacific SST rises quickly to form into a U pattern, as if it were austral fall, when Q_{SW} is prescribed with the January conditions. A vague

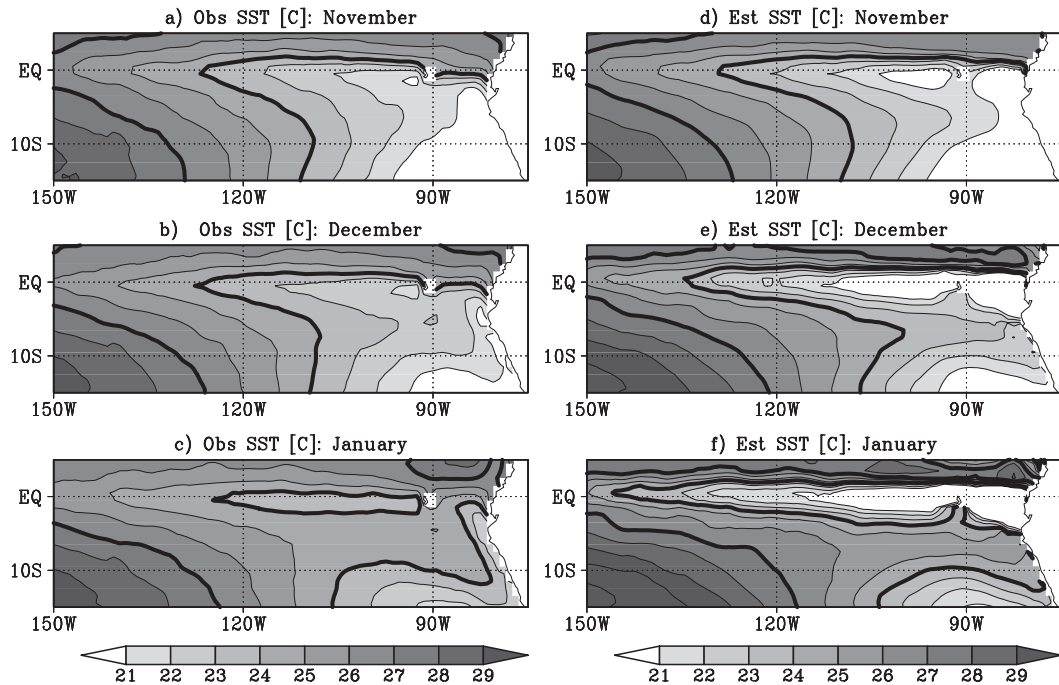


FIG. 4. Observed monthly climatologies of SST ($^{\circ}\text{C}$) for (a) November, (b) December, and (c) January. (d)–(f) Same as (a)–(c), but for estimated SST from the control run of the austral fall experiment. SSTs of 24° and 27°C are highlighted by thick contours.

resemblance of the U pattern is also seen in the ADV fixed run.

Figure 7 illustrates the spatial distribution of SST estimated from different runs. In the austral fall experiment (left column), the southeast Pacific warm band is reproduced in all runs except the SW fixed one. All of these results are reversed in the boreal fall experiment (right column of Fig. 7). Only the SW fixed run allows a salient (but artificial) warm band to develop. The ADV fixed run yields faint evidence of the southeast Pacific warm band. All of the other runs from the boreal fall experiment lack robust evidence for the warm band.

It is inferred from these results that the southeast Pacific warm band is promoted or suppressed primarily by the seasonal cycle of the absorbed shortwave flux. The contribution of any other heat flux is negligible or at most secondary. Ocean advection is most dominant among the secondary factors and may have some visible impact.

5. Discussion

The analysis in section 4 focused on the temporal evolution of SST in the tropical southeast Pacific. Discussed next is what determines the geographical structure of the southeast Pacific warm band, followed by the effects of cloud shielding, interannual variability, and implications for modeling studies.

a. Spatial structure of the warm band

Figure 8 is the regional map of the January mean heat fluxes estimated by the control run from the austral fall experiment. The total heat budget (Fig. 8a), or the RHS of (1) as a whole, for this month implies a warming tendency of the ocean surface everywhere outside the narrow equatorial cold tongue. The cold tongue is apparently fed by the equatorial upwelling (Fig. 8f). To the south of the cold tongue, the total heat flux is about 60 W m^{-2} around 120°W and gradually increases eastward until it reaches $\sim 100 \text{ W m}^{-2}$ or larger off the South American coast. This local enhancement of the total heat flux presumably explains the 90°W maximum observed in the southeast Pacific warm band.

The absorbed shortwave flux (Fig. 8c) is by far largest in magnitude among the heat fluxes and accounts for nearly all of the thermal energy absorbed into the ocean mixed layer. All other fluxes primarily have cooling effects that compete against the absorbed shortwave heating. The absorbed shortwave flux shows a strong meridional gradient, as expected from the seasonal solar radiation, as well as a moderate zonal variability that is caused by reflecting clouds and the westward-deepening mixed layer. The latent heat flux (Fig. 8d) has a large-scale zonal gradient, which is probably responsible for the eastward increase in the total heat flux mentioned earlier. The abrupt drop in the total heat flux at the very

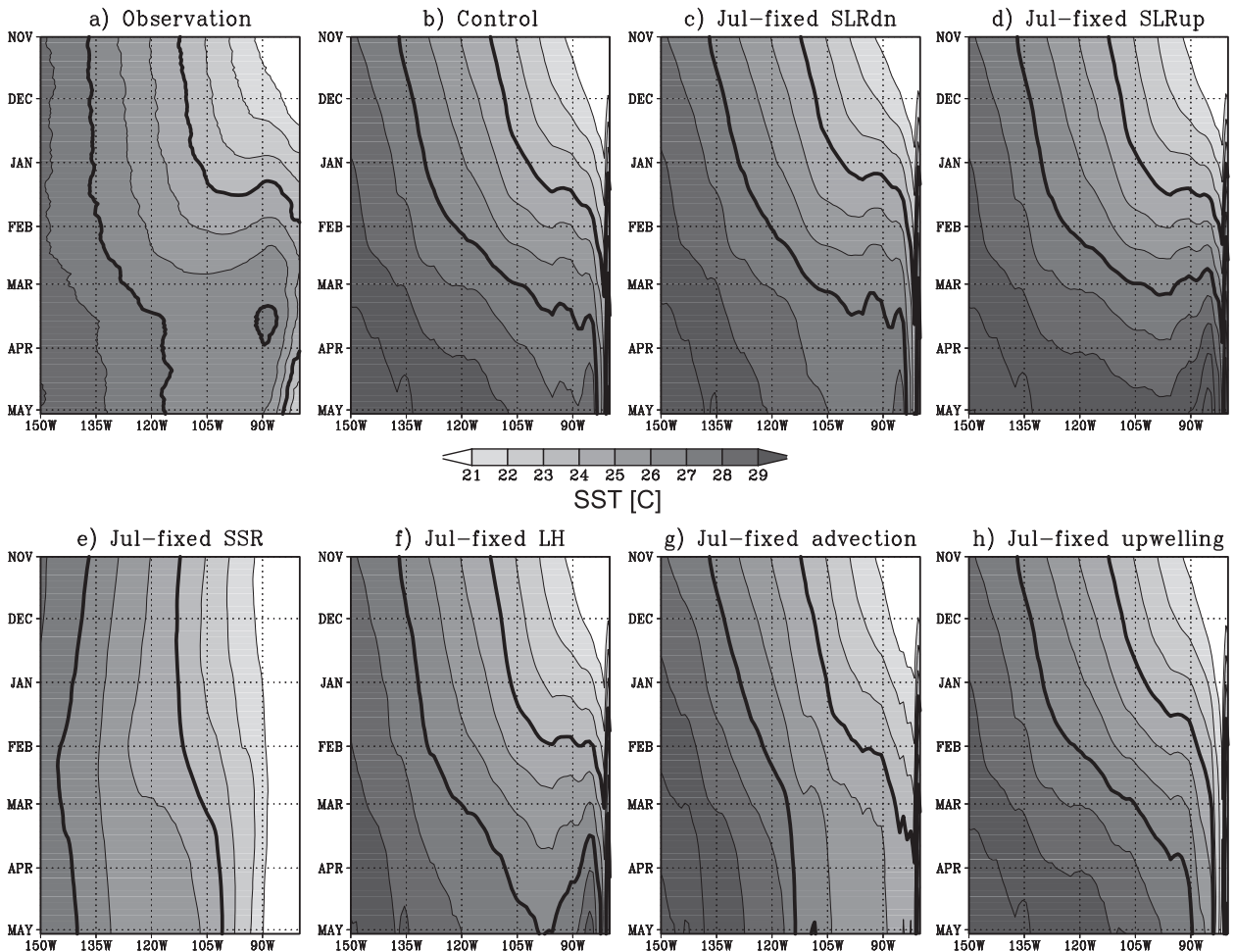


FIG. 5. Hovmöller diagrams of SST averaged over 12.5°–2.5°S from (a) observation and (b)–(h) different runs from the austral fall experiment: (b) control, (c) LW \downarrow fixed, (d) LW \uparrow fixed, (e) SW fixed, (f) LH fixed, (g) ADV fixed, and (h) UpW fixed runs. SSTs of 24° and 27°C are highlighted by thick contours. See section 4a for details on experimental setup.

eastern end of the ocean is ascribed to coastal upwelling. Spatial inhomogeneity in Q_{adv} in the vicinity of the equator is probably related to the tropical instability wave.

Figure 9 illustrates the July climatology of the surface heat fluxes. The seasonal contrast between January and July is most prominent in the absorbed shortwave flux. There are areas showing notable seasonal variation in some of the other fluxes, for example, well-known stratocumulus regions off the South American coast modulating Q_{LW} (Fig. 9b), but the amplitude of these variation (or difference between the July and January climatologies), which is $\sim 50 \text{ W m}^{-2}$ at most, are much less than the overall changes in the total heat budget. This value is largely dominated by the absorbed shortwave flux, which reduces by more than 100 W m^{-2} from January to July in the tropical southeast Pacific. As a result, the total heat flux changes sign across the tropical southeast Pacific, preventing the warm band from developing in this season.

In this study, sensitivity to the individual heat fluxes is investigated without a possible linkage between different fluxes taken into account. Different flux terms, however, are generally not independent of each other. For instance, an enhanced solar flux would reinforce the wind blown into the convergence zone in response to an increase of SST, resulting in a change of advective and latent heat fluxes. An example was found in some coupled climate models (de Szoeke and Xie 2008), where a northerly wind bias on the equator leads to a cold SST bias there when the south ITCZ is too strong. The inclusion of such secondary effects in the sensitivity study would possibly introduce additional impacts on the mixed layer heat budget.

b. Cloud impact on the shortwave flux

Past studies (Mitchell and Wallace 1992; Philander et al. 1996) argued that marine stratocumulus helps keep

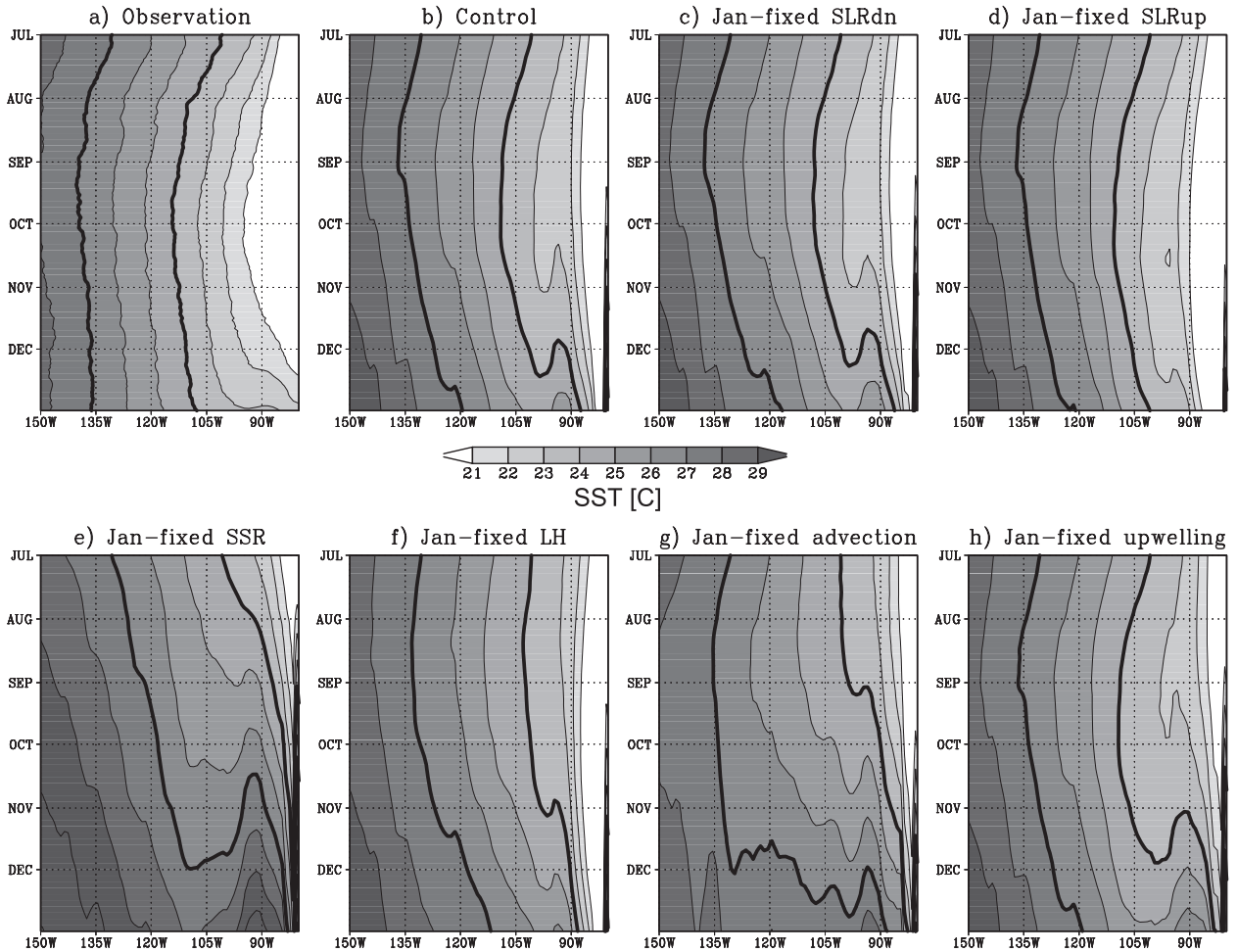


FIG. 6. Same as Fig. 5, but from the boreal fall experiment.

SST relatively low in the tropical southeast Pacific and thus is partially responsible for the meridional asymmetry of the ITCZ. Cloud impacts on the absorbed shortwave flux are evaluated in this subsection. To this end, a “clear-sky” run is performed using the cloud-free shortwave and longwave fluxes provided by the HERB dataset, which is calculated daily with all clouds removed. The run is initialized on 1 July, as done for the boreal fall experiment. The clear-sky run represents a hypothetical world where the shortwave penetrates down to the ocean surface without being scattered by clouds at all. The increase of insolation resulting from the absence of clouds is somewhat offset by a reduction of downwelling longwave flux in the net heat budget.

Figure 10 shows southeast Pacific SST from the clear-sky run together with the control run. It is evident that the southeast Pacific warm band would develop even in boreal summer and fall, although not as strong as the austral fall event, if it were not for cloud-shielding effects. In a regional ocean–atmosphere model run by Xie

et al. (2007), the annual mean SST in the south ITCZ area was found to increase by 2° – 3° C if overlying clouds were removed. As a result, this sea surface warming in the absence of clouds gives rise to a warm band south of the equator as seen in the present result. It is noted that cloud impacts on the radiative fluxes are not strongly dependent on season but are more or less constant throughout the year. Figure 11 demonstrates that the seasonal variation of Q_{SW} is virtually parallel between the clear-sky (dotted) and control (solid) runs, differing only by an offset of $\sim 20 \text{ W m}^{-2}$ and day-to-day fluctuations. When the longwave contribution is subtracted from the clear-sky Q_{SW} to delineate the net radiative effect (dashed), the offset is reduced to 10 – 15 W m^{-2} but is still consistent year-round. It follows that the seasonality of the southeast Pacific warm band is essentially driven by the annual cycle of insolation, with its magnitude reduced constantly by clouds, which peaks from mid-October to late February for latitudes of the study area.

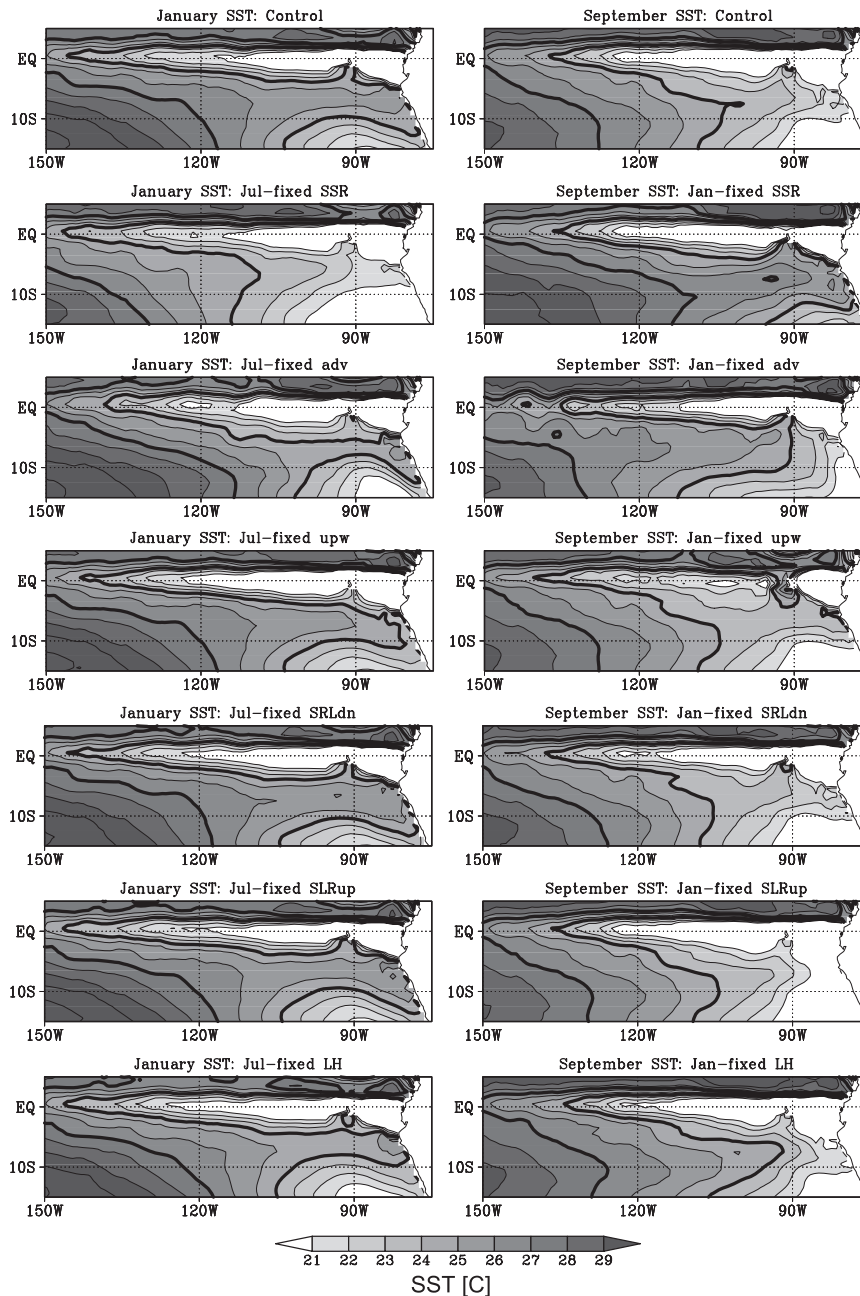


FIG. 7. (left) January mean SST ($^{\circ}\text{C}$) for (from top to bottom) the control, SW fixed, ADV fixed, UpW fixed, LW \downarrow fixed, LW \uparrow fixed, and LH fixed runs from the austral fall experiment. SSTs of 24° and 27°C are highlighted by thick contours. (right) Same as left, but for September mean SST for runs from the boreal fall experiment.

Figure 11 also shows Q_{SW} for the northeast Pacific ITCZ (2.5° – 12.5°N , 150° – 80°W). The magnitude of Q_{SW} is smaller than in the southeast Pacific mainly because the mixed layer is shallower north of the equator and therefore absorbs less shortwave flux (see the appendix and Fig. A2). The annual cycle of insolation is also slightly weaker in amplitude in the Northern Hemisphere than

in the Southern Hemisphere because the earth passes through the perihelion in austral summer in the present-day orbit. The reduction in Q_{SW} resulting from cloud shielding is more dramatic in the north ITCZ than in its southern counterpart. In general, the north ITCZ is exposed to relatively moderate shortwave flux compared to the south ITCZ. This result is somewhat counterintuitive,

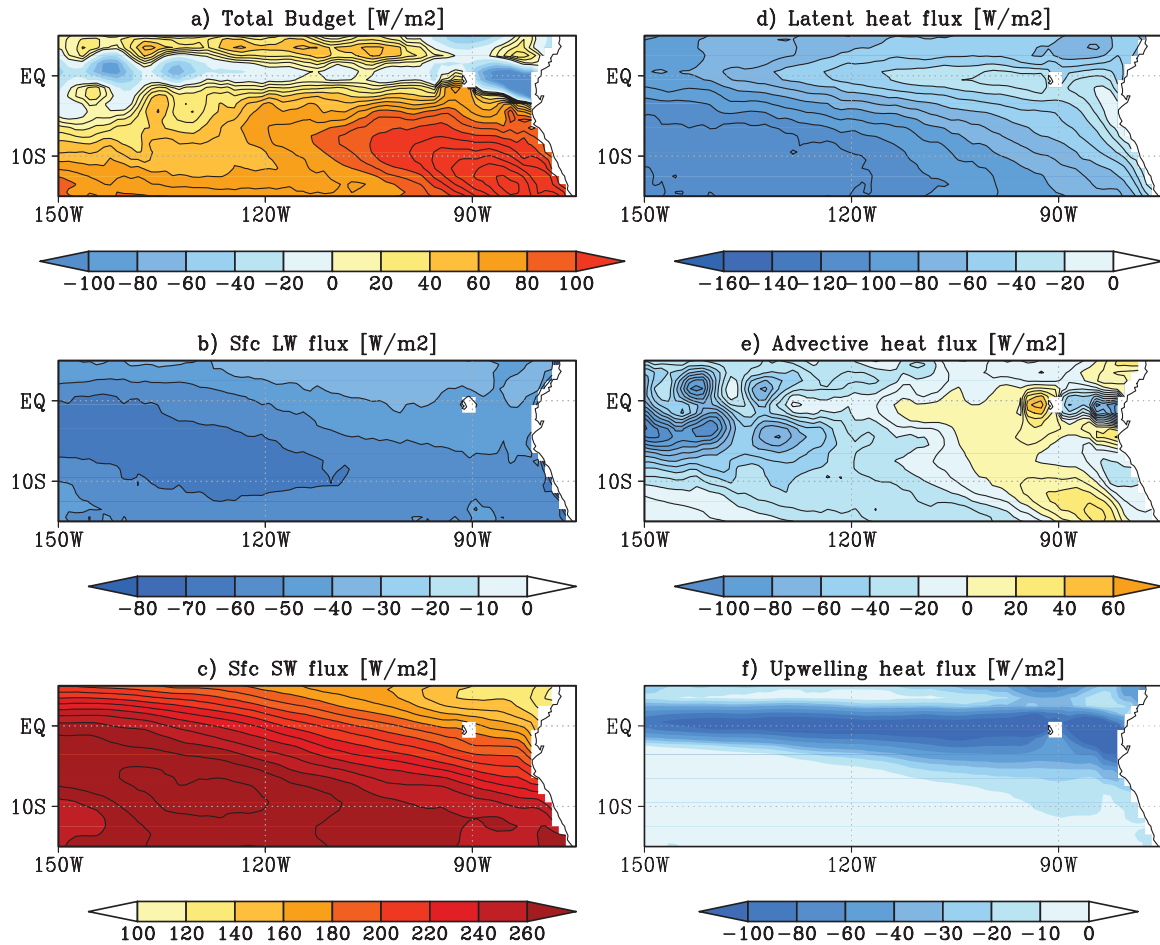


FIG. 8. January mean heat fluxes (W m^{-2}) estimated from the austral fall experiment (control run): (a) all fluxes summed together, (b) net surface longwave flux (Q_{LW}), (c) shortwave flux absorbed into the ocean mixed layer (Q_{SW}), (d) surface latent heat flux (Q_{LH}), (e) ocean advective heat flux (Q_{adv}), and (f) ocean upwelling heat flux (Q_{upw}). Positive (negative) values indicate warming (cooling) tendency. Color shade is scaled as indicated. Contour interval is 10 W m^{-2} except for negative fluxes in (a) and (f), where contours are omitted for clarity.

given that the total heat flux north of the equatorial cold tongue stays positive in both summer and winter (see Figs. 8 and 9). It is beyond the scope of the present study to explore this problem, whereas it is potentially important in relevance to the persistence of the northeast Pacific ITCZ.

c. Dynamics of the growth of the south ITCZ

We have seen in section 3 that the growing processes of the south ITCZ involve a few distinct stages. The emergence of the southeast Pacific warm band is followed by an increase in the population of shallow cumulus and eventually by the onset of vigorous deep convection. The continuous development of surface convergence and moisture also accompanies the growth of the south ITCZ. It is noteworthy that surface convergence starts rising much earlier than the onset of deep

convection. Liu and Xie (2002) pointed out that a weak south ITCZ is observed outside the period when the double ITCZ is visible in deep convective clouds. They attributed the weak ITCZ, without cumulus dynamics involved, to the deceleration of surface wind in response to an SST gradient flanking the southeast Pacific warm band. The moisture increase resulting from surface convergence and continuing sea surface warming would generate thermodynamic conditions favoring moist convection in an area that is otherwise capped by the persistent trade inversion. The seasonal migration of solar zenith angle makes Q_{SW} decline after March (Fig. 11). This leads to the dissipation of the southeast Pacific warm band, which disables the further maintenance of the south ITCZ.

A similar evolutionary sequence, that is, prior sea surface warming followed by tropospheric moistening and

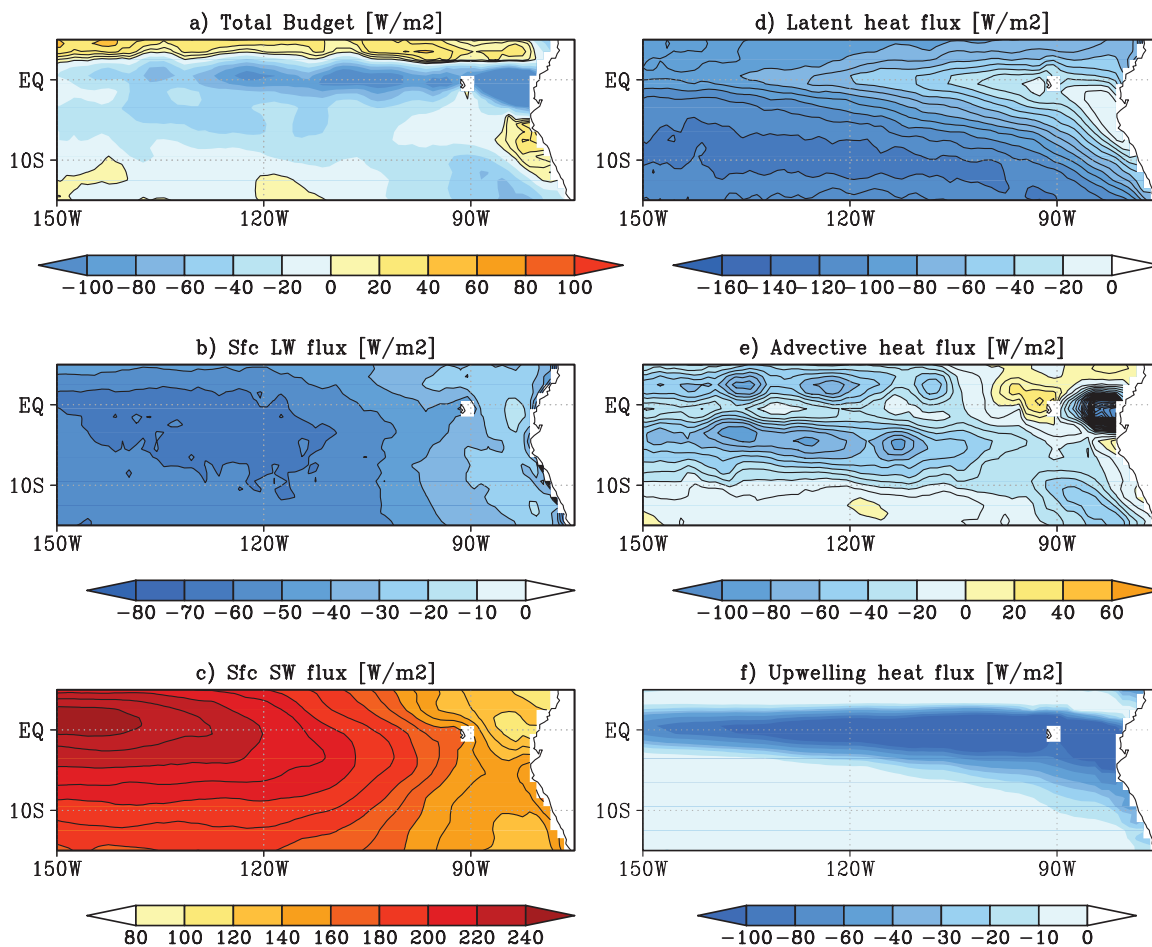


FIG. 9. Same as Fig. 8, but July mean heat fluxes estimated from the boreal fall experiment.

cloud deepening, is often documented in the context of intraseasonal oscillations (Lin and Johnson 1996; Zhang 1996; Kiladis et al. 2005; Masunaga et al. 2006; Benedict and Randall 2007). Because the south ITCZ is neither oscillating nor propagating, wave dynamics do not account for its physical origins, but the resemblance is so apparent that it may suggest that some generic processes are common to the tropical oscillations and the south ITCZ. For instance, shallow cumulus clouds developing on the leading edge of the Madden–Julian oscillation arguably promote the moisture transfer from the boundary layer to the free troposphere, preconditioning a convective burst to come (Kemball-Cook and Weare 2001). It is possible that the early increase of shallow cumulus population may help to convectively activate the south ITCZ as well.

A regional coupled ocean–atmosphere model simulation (Xie et al. 2007) showed that the cloud base is decoupled from the atmospheric mixed layer beneath over the southeast Pacific from February through April. This suggests that stratocumulus clouds should be broken

up into shallow cumulus during these months, consistent with the present observational evidence. An increase of shallow cumulus accompanying the dissipation of stratocumulus clouds leads to an enhancement of solar radiation reaching the sea surface. De Szoeke et al. (2006) found that the south Pacific warm band does not develop, and thus neither does the south ITCZ, in a coupled model when the shallow convection parameterization is disabled. The transition from stratocumuli to shallow cumulus is probably an additional factor that promotes the development of the warm band.

d. Interannual variability

While the primary focus of this paper is limited to climatological aspects of the east Pacific double ITCZ, year-to-year variability is briefly explored here. Figure 12 depicts bimonthly (March and April) mean SST and the deep storm fraction for each year studied. The south ITCZ is consistently observed every year in these months, but markedly varies in strength from year to year. A salient south ITCZ develops in 2000, 2001, 2004, and 2006,

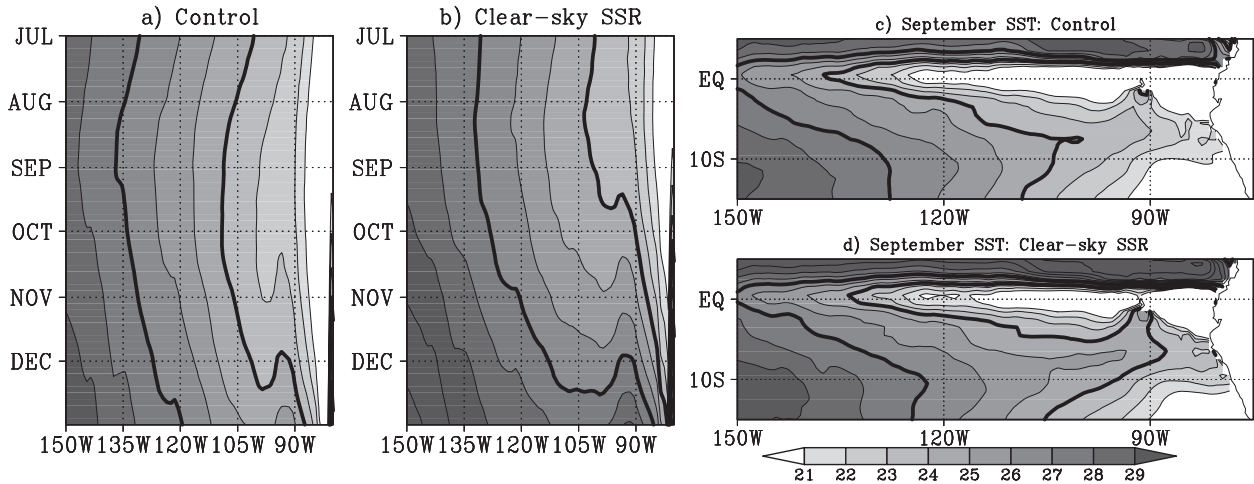


FIG. 10. Hovmöller diagram of SST averaged over 12.5°–2.5°S for the (a) control run and (b) clear-sky run, and the regional map of September mean SST for the (c) control run and (d) clear-sky run from the boreal fall experiment. SSTs of 24° and 27°C are highlighted by thick contours.

while it is relatively weak in 2002 and 2007 and barely recognizable in 2003, as noted by Gu et al. (2005), and 2005. The southeast Pacific warm band is discernible even in the year with the faintest ITCZ, although it is less mature than in other years. The magnitude of the southeast Pacific warm band is closely related to the strength of the south ITCZ in interannual variability as also argued by Zhang (2001).

We have shown that the primary driver of the southeast Pacific warm band is the absorbed shortwave flux. Figure 13 plots monthly mean Q_{SW} and the rate of SST change or $dSST/dt$ averaged over the tropical southeast Pacific. The time series demonstrates that the annual cycles of Q_{SW} and $dSST/dt$ are in phase, consistent with the expectation that the rate of SST change is controlled dominantly by Q_{SW} in Eq. (1). A closer examination of Fig. 13 reveals that the amplitude of the annual cycle is also coherently modulated where $dSST/dt$ is positive,

that is, during the developing stage of the warm band. In contrast, coherent amplitude modulation is virtually absent when $dSST/dt$ is negative. This contrast is confirmed by the scatterplot of Q_{SW} and $dSST/dt$. When $dSST/dt$ is greater than zero, $dSST/dt$ is tightly coupled with Q_{SW} , showing a clear positive correlation. The correlation is looser for $dSST/dt < 0$. It follows that the growth of the southeast Pacific warm band is modulated by Q_{SW} not only in climatology but also in individual years. A larger (smaller) Q_{SW} in austral summer results in a warmer (cooler) SST in the tropical southeast Pacific, which in turn leads to a stronger (weaker) south ITCZ in the subsequent austral fall. On the other hand, the magnitude of sea surface cooling tendency in boreal summer does not closely reflect the year-to-year variation of the incoming shortwave flux.

Because the seasonality of insolation is strictly invariable from a year to another on a decadal time scale,

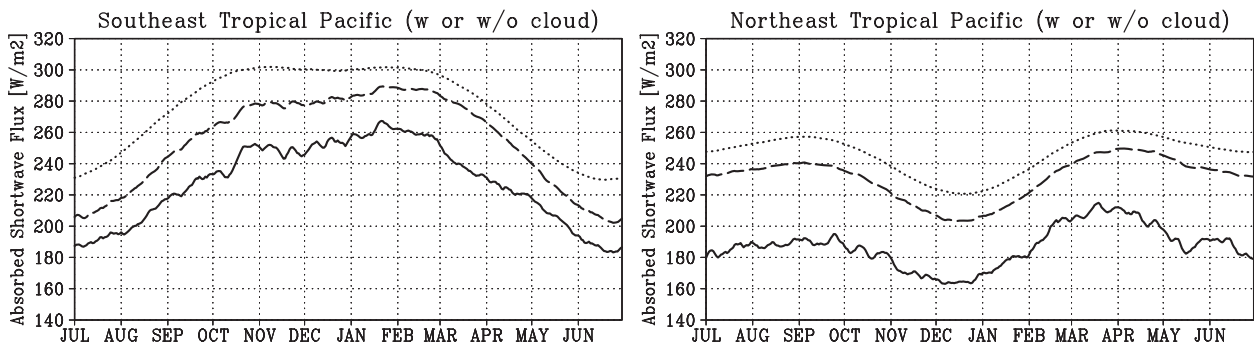


FIG. 11. Daily climatology of control Q_{SW} (solid), clear-sky Q_{SW} (dotted), and clear-sky Q_{SW} offset by the cloud longwave impact (dashed) averaged over (left) southeast tropical Pacific (12.5°–2.5°S, 150°–85°W) and (right) northeast tropical Pacific (2.5°–12.5°N, 150°–80°W).

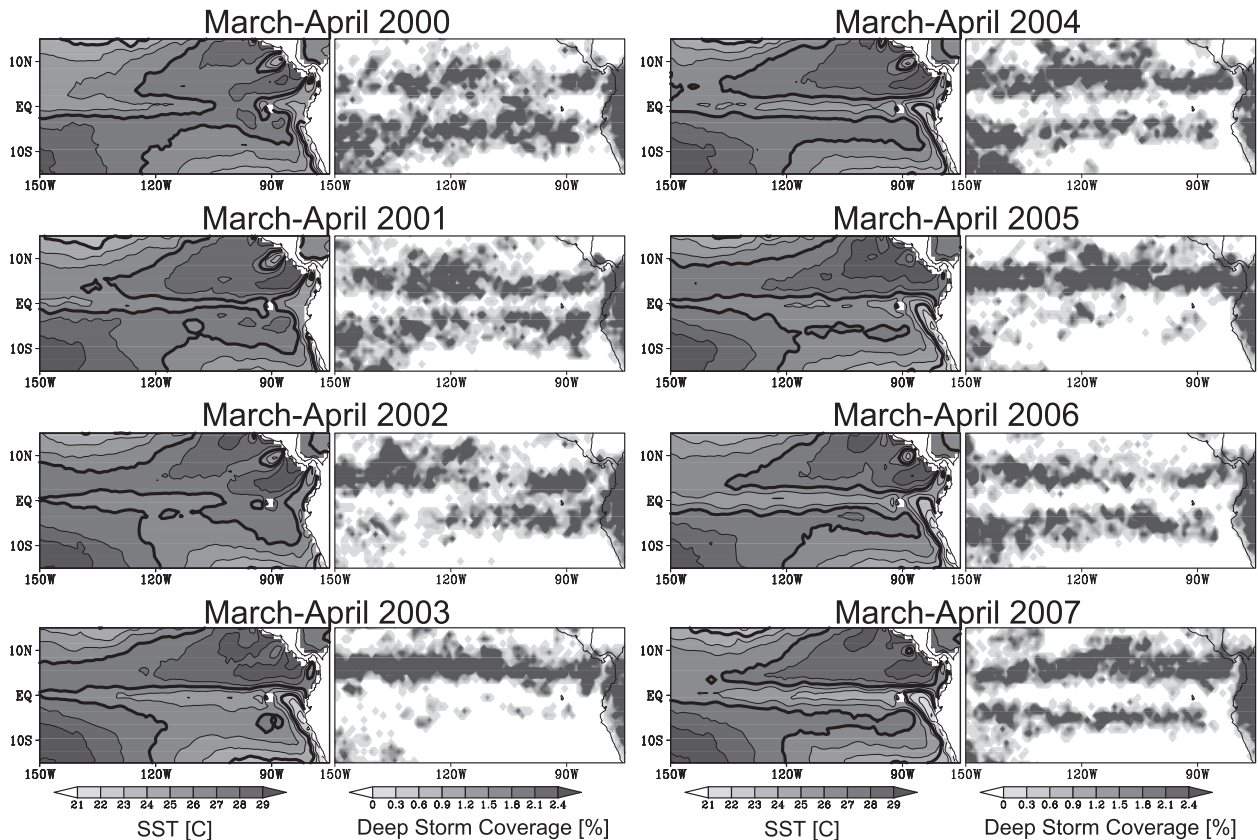


FIG. 12. Bimonthly (March and April) mean SST ($^{\circ}\text{C}$) and deep storm coverage (%) for each year from (top left) 2000 to (bottom right) 2007. SSTs of 24° and 27°C are highlighted by thick contours.

the interannual variation of Q_{SW} is controlled by clouds. Such cloud variability is, however, not the only factor governing the interannual variation of the double ITCZ. The largest source of interannual variability that has not been tested in this study is probably ENSO. It is known that the east Pacific double ITCZ is either faint or absent during El Niño events (Zhang 2001). Various effects, including anomalous ocean upwelling, would be needed to explain the key factors that suppress the southeast Pacific warm band in El Niño years. Unfortunately, it is difficult to extract robust ENSO signals from the study period of the present work. The ENSO impacts on the southeast Pacific warm band, and its possible feedback to ENSO, are left for future studies.

e. Implications for coupled climate models

It has been recognized for years that coupled ocean-atmosphere general circulation models often have difficulties in simulating realistic SST in the tropical east Pacific. While a limited number of coupled models are successful in reproducing the seasonality of east Pacific SST and ITCZ, some models tend to have a persistent double ITCZ and some others exhibit a seasonally mi-

grating ITCZ across the equator (Mechoso et al. 1995; Dai 2006; de Szoeke and Xie 2008). Causes for these errors are highly complicated and have yet to fully understand. Nevertheless, it would be beneficial to briefly discuss the current findings in light of known problems in coupled ocean-atmosphere modeling.

We have seen that the absorbed solar radiation is the key factor controlling the seasonality of the south ITCZ and that cloudiness is required to suppress the southeast Pacific warm band in austral winter and spring. Other factors, which may not have been well recognized before in conjunction with the south ITCZ, include the mixed layer depth and mixed layer absorptivity of shortwave radiation. The mixed layer depth (H_{ml}) could exert competing effects on the ocean heat budget. While an increase in H_{ml} lowers the SST tendency for a given magnitude of the total heat flux [see Eq. (1)], it enhances the absorbed shortwave flux in the tropical east Pacific where the mixed layer is shallow [see Eq. (A16)]. The latter effect can be large enough to give rise to a spurious warm band in the southeast Pacific depending on the choice of H_{ml} (not shown). An overestimated shortwave absorptivity would cause the same SST bias. A misrepresentation

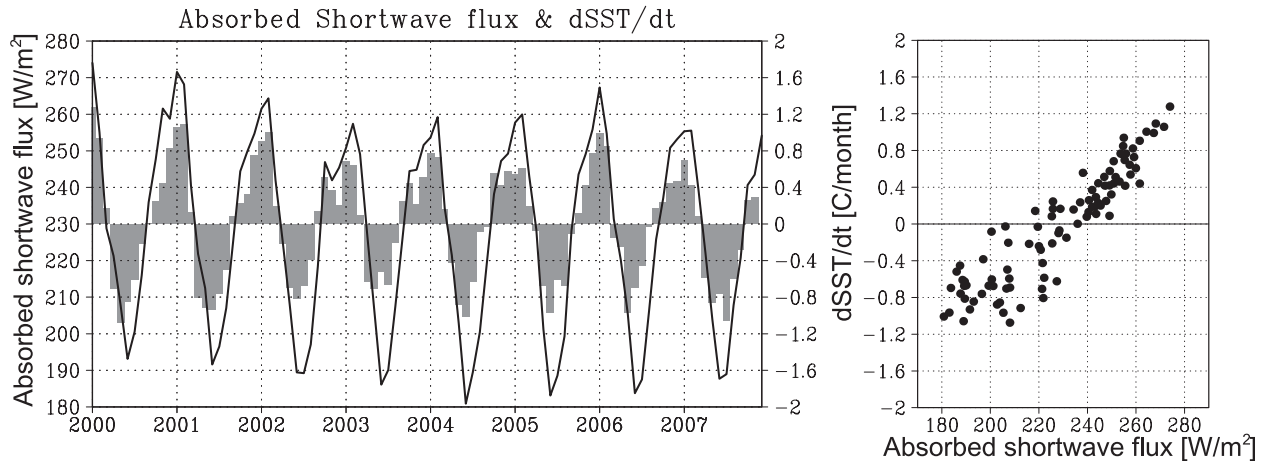


FIG. 13. Regional mean Q_{SW} ($W m^{-2}$) and the rate of SST change ($dSST/dt$; $^{\circ}C month^{-1}$) for the tropical southeast Pacific (12.5° – $2.5^{\circ}S$, 150° – $85^{\circ}W$). (left) Monthly time series of Q_{SW} (solid curve, labeled on the left ordinate) and $dSST/dt$ (shaded bars, labeled on the right ordinate). (right) Scatterplot of Q_{SW} (abscissa) and $dSST/dt$ (ordinate). All values are monthly mean.

of these parameters might be partly responsible for the double ITCZ error in some coupled models.

The double ITCZ error has given way to an alternating ITCZ error in recent coupled models, where the north ITCZ weakens too much during the time when the south ITCZ strengthens (de Szoeke and Xie 2008). Interestingly, such seasonal migration of the ITCZ is what would be expected if the north ITCZ were dominated by the same dynamics as those controlling the south ITCZ. Identifying causes for the alternating ITCZ error requires further understanding of the mechanisms that sustain the north ITCZ perpetually against the seasonal weakening of insolation.

6. Summary

The present study is aimed at determining the growth mechanism of the east Pacific double ITCZ in austral fall. Satellite measurements from the TRMM and QuikSCAT were analyzed to derive the 8-yr climatologies of SST, surface convergence, CWV, shallow and deep precipitating clouds, and the surface heat fluxes from 2000 to 2007. The initial signature of the south ITCZ emerges in SST, referred to as the southeast Pacific warm band, as early as in January. A pronounced feature of the warm band is a local SST maximum around $90^{\circ}W$, resulting from the sum of different surface heat fluxes having different signs and competing geographical patterns. Surface convergence and CWV gradually develop along the southeast Pacific warm band. The population of shallow cumulus starts growing to form the south ITCZ in February, a month earlier than vigorous deep convection that finally organizes in the south ITCZ in March. The double ITCZ therefore does not emerge abruptly in

austral fall, but results from a series of distinctive evolutionary stages in the preceding months, initiated by SST in the previous austral summer.

Simple experiments were carried out in order to diagnose the key factors that give rise to the southeast Pacific warm band. In the experiments, the heat budget of the ocean mixed layer is calculated with the surface heat fluxes (longwave, shortwave, latent heat, advection, and upwelling), all of which are derived from satellite observations. The results suggest that the absorbed shortwave flux primarily drives the southeast Pacific warm band, enhanced to a lesser extent by the ocean advection. Insolation remains near the annual maximum from austral summer through late February for a latitudinal range of the south ITCZ, resulting in a peak in tropical southeast Pacific SST and the south ITCZ in March. It is now obvious why the double ITCZ is absent in boreal fall: the incoming shortwave flux is minimum in the preceding solstice season, and thus incapable of maintaining a warm ocean surface in the Southern Hemisphere. The heat budget calculation shows that the ocean mixed layer exhibits a cooling tendency in July, where the shortwave flux is overwhelmed by negative fluxes such as the latent heat and longwave fluxes.

Cloud impacts on the shortwave flux in the tropical east Pacific have also been quantified. Clouds offset the net radiation by 10 – $15 W m^{-2}$ throughout the year in the tropical southeast Pacific. This offset is so large that the warm band would also develop in boreal fall if reflecting clouds did not exist. It was also found that a year with a robust (faint) southeast Pacific warm band has a strong (weak) south ITCZ, supporting the strong SST influence on the ITCZ. The ENSO modulation of the austral fall double ITCZ would require a longer period

to study than the current analysis and thus is not discussed in this paper.

The meridional asymmetry of the east Pacific ITCZ has generally been explored in the literature by asking why the Southern Hemisphere lacks a permanent ITCZ (Mitchell and Wallace 1992; Xie and Philander 1994; Philander et al. 1996). The present findings suggest that the seasonal preference of the south ITCZ is a natural consequence of the annual cycle of insolation. This supports the model result of Wang and Wang (1999) that the annual march of solar forcing is crucial for maintaining the meridional asymmetry of the ITCZ. It is, however, not completely clear why SST remains high even in local winter north of the equator. The real mystery might be not why the south ITCZ is transient but why the ITCZ could persist all the year around in the northeast Pacific.

Acknowledgments. The TRMM PR (2A25) and VIRS (1B01) datasets were provided by the Japan Aerospace Exploration Agency (JAXA) Earth Observation Research Center (EORC). The TMI-retrieved SST and CWV datasets are produced and distributed by the Remote Sensing Systems (<http://www.ssmi.com>). The QuikSCAT SeaWinds ocean wind vector data and OSCAR surface current product were obtained from the Physical Oceanography Distributed Active Archive Center (PO.DAAC) at the NASA Jet Propulsion Laboratory, Pasadena, California (<http://podaac.jpl.nasa.gov>). The Tropical Atmosphere/Ocean (TAO) Project Office of the National Oceanic and Atmospheric Administration (NOAA)/Pacific Marine Environmental Laboratory (PMEL) provided ocean buoy data. The WOA05 temperature data were obtained from the NOAA/National Oceanographic Data Center. The mixed layer depth dataset was downloaded (<http://www.lodyc.jussieu.fr/~cdblod/ml.d.html>). This work is supported by the Ministry of Education, Culture, Sports, Science, and Technology (MEXT) Grant-in-Aid for Young Scientists No. 20740269. The HERB dataset was generated under the support of National Aeronautics and Space Administration (NASA) Energy and Water Cycle Study (NEWS) Grant NAG06GC46G.

APPENDIX

Method for Ocean Surface Flux Estimate

a. Latent heat flux

The latent heat flux through evaporation from the ocean surface is estimated by use of the bulk formula,

$$Q_{\text{LH}} = \rho_a L_v C_E [q_v - q_v^*(T_s)] |\mathbf{u}_{10}|, \quad (\text{A1})$$

where ρ_a , L_v , q_v , $q_v^*(T)$, and \mathbf{u}_{10} are the dry air density (1.22 kg m^{-3}), vapor latent heat per unit mass ($2.5 \times 10^6 \text{ J kg}^{-1}$), vapor mixing ratio, saturation vapor mixing ratio for temperature T , and the wind velocity at 10 m above the sea surface, respectively. The saturation vapor mixing ratio is reduced by 2% from the value expected from the Clausius–Clapeyron relation to take the salinity effect into account. The neutral, 10-m bulk transfer coefficients are obtained from the empirical formulas derived by Large et al. (1994),

$$10^3 C_E = 34.6 C_D^{1/2}, \quad (\text{A2})$$

where

$$10^3 C_D = \frac{2.70 \text{ m s}^{-1}}{|\mathbf{u}_{10}|} + 0.142 + \frac{|\mathbf{u}_{10}|}{13.09 \text{ m s}^{-1}}. \quad (\text{A3})$$

Microwave radiometer measurements provide SST required for (A1), but not q_v at any specified vertical level. Existing studies to estimate latent heat flux from satellite data have explored a variety of algorithms to derive q_v (Chou et al. 1995; Jourdan and Gautier 1995; Schulz et al. 1997; Curry et al. 1999; Kubota et al. 2002, and references therein). In this study, a simple formula is established, where q_v is regressed from CWV and SST. Figure A1a shows the scatterplot of in situ water vapor density, or $\rho_a q_v$, against CWV. The in situ water vapor density is obtained from relative humidity data acquired at nine of the Tropical Atmosphere Ocean (TAO) arrayed bouys that are moored in the southeast Pacific (i.e., 8°S, 5°S, and 2°S and 125°W, 110°W, and 95°W). Satellite overpasses are extracted for each selected buoy to pair the in situ water vapor with CWV.

Figure A1a appears to suggest that the in situ water density is not accurately determined by CWV alone. An additional constraint of underlying SST, however, breaks the plot down into distinct groups. Two example cases of $27^\circ \pm 0.5^\circ\text{C}$ and $21^\circ \pm 0.5^\circ\text{C}$ are shown by dots and crosses, respectively. The scatter turns out to be further reduced (and almost linearly correlated) when the ordinate is redefined with

$$H_v = \frac{W}{\rho_a q_v}, \quad (\text{A4})$$

where W designates CWV (Fig. A1b). Note that H_v represents the water vapor scale height when the vertical profile of $\rho_a q_v$ is approximated to be exponential. A bivariate linear regression is applied to H_v as a function of CWV and SST. The resultant empirical formula is

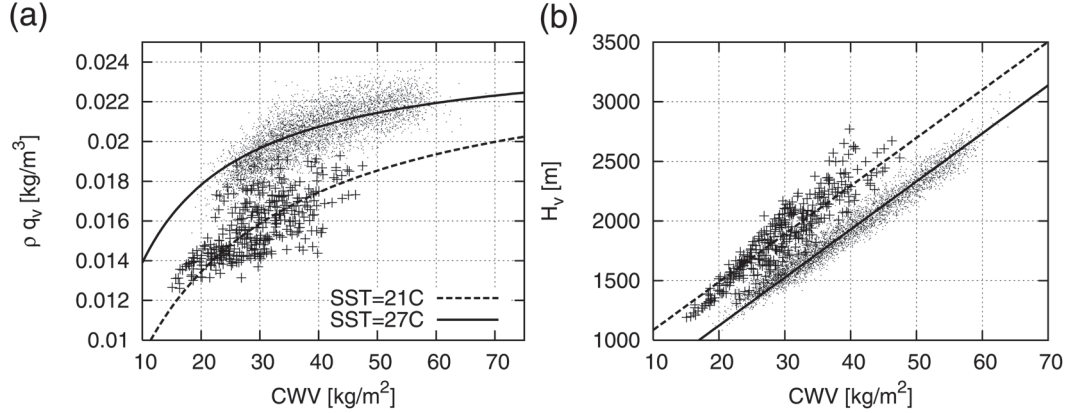


FIG. A1. (a) Scatterplot of in situ water vapor density or $\rho_a q_v$ against CWV for different SSTs. Dots and crosses denote SSTs of 27° and 21°C, respectively, with other SSTs omitted for clarity of presentation. (b) Same as (a), but for H_v or $CWV/\rho_a q_v$ instead of $\rho_a q_v$. Solid and dashed lines are regressed curves for SSTs of 27° and 21°C, respectively. See text for details.

$$\frac{H_v}{[\text{m}]} = 1961 + 40.3 \times \frac{W}{[\text{kg m}^{-2}]} - 60.9 \times \frac{T_s}{[^\circ\text{C}]}, \quad (\text{A5})$$

or

$$\frac{\rho_a q_v}{[\text{kg m}^{-3}]} = \frac{\frac{W}{[\text{kg m}^{-2}]}}{\left(1961 + 40.3 \times \frac{W}{[\text{kg m}^{-2}]} - 60.9 \times \frac{T_s}{[^\circ\text{C}]}\right)}, \quad (\text{A6})$$

which is delineated in Fig. A1. The latent heat flux is calculated using (A1) and (A6) for given CWV, SST, and $|\mathbf{u}_{10}|$, all of which are provided by satellite observations.

b. Ocean advection and upwelling fluxes

The advective heat transport in the ocean mixed layer Q_{adv} is derived from the satellite-derived surface current (OSCAR product) and SST. The OSCAR current is defined as the mean velocity averaged between the surface and 30-m depth. The assumption of a constant depth at 30 m may introduce a minor error in the present analysis because the mixed layer depth varies from 10 to ~ 70 m in the study domain. Uncertainties in the horizontal advection, however, are not critical for the heat budget analysis of the east Pacific warm bands, where radiative and latent heat fluxes are virtually in balance (Xie 1994). The mixed layer mass transport \mathbf{M}_{ml} is

$$\mathbf{M}_{\text{ml}} = \rho_w H_{\text{ml}} \mathbf{u}, \quad (\text{A7})$$

where \mathbf{u} is the current velocity. The advective heat flux is then evaluated as

$$Q_{\text{adv}} = -C_{p,w} \mathbf{M}_{\text{ml}} \cdot \nabla T_s, \quad (\text{A8})$$

An annual climatology of H_{ml} is adopted from de Boyer Montégut et al. (2004) with a variable density criterion corresponding to $\Delta T = -0.2^\circ\text{C}$ applied against the reference depth at 10 m. A variable density criterion is used instead of a simple temperature threshold so that a barrier layer, known to develop in the tropical convergence zones, is detected and separated (Sprintall and Tomczak 1992). Figure A2a shows the regional map of H_{ml} , where H_{ml} deepens southwestward in the tropical east Pacific.

Given the wind stress vector $\boldsymbol{\tau}$ estimated from QuikSCAT wind,

$$\boldsymbol{\tau} = \rho_a C_D |\mathbf{u}_{10}| \mathbf{u}_{10}, \quad (\text{A9})$$

the Ekman mass transport $\mathbf{M}_E \equiv (M_{E,x}, M_{E,y})^T$ is evaluated from

$$r_s M_{E,x} - f M_{E,y} = \tau_x, \quad (\text{A10})$$

$$r_s M_{E,y} + f M_{E,x} = \tau_y, \quad (\text{A11})$$

where r_s is the drag coefficient, f the Coriolis parameter, and τ_x and τ_y the zonal and meridional components of $\boldsymbol{\tau}$, respectively. The drag coefficient was empirically estimated by Lagerloef et al. (1999) to be $2.15 \times 10^{-4} \text{ m s}^{-1}$ for the Ekman layer with a depth of 32.5 m. In the present formulation, r_s is defined per unit depth and is given as $2.15 \times 10^{-4}/32.5$ or $6.62 \times 10^{-6} \text{ s}^{-1}$. The drag term is essential in the vicinity of the equator, where \mathbf{M}_E would otherwise diverge to infinity as f diminishes to zero. Upwelling velocity w_E is

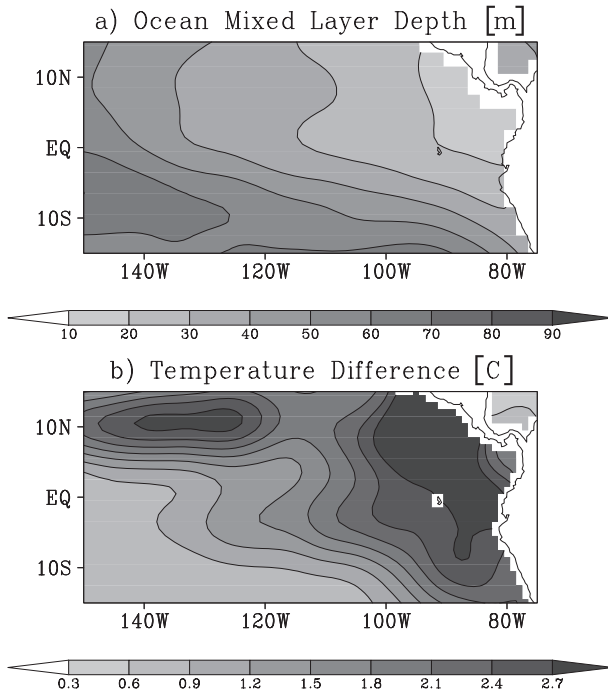


FIG. A2. The annual climatologies of (a) mixed layer depth (H_{ml}) and (b) temperature difference between the mixed layer and upwelling water from beneath (ΔT_E).

$$w_E = \frac{1}{\rho_w} \nabla \cdot \mathbf{M}_E, \quad (\text{A12})$$

and the upwelling heat flux is evaluated as

$$Q_{upw} = -\rho_w C_{p,w} w_E \mathcal{H}(w_E) \Delta T_E, \quad (\text{A13})$$

where \mathcal{H} is the Heaviside function and ΔT_E represents the temperature difference between mixed layer water and upwelling water from beneath. In this work, ΔT_E is prescribed from the annual climatology of local temperature difference between the two reference depths, that is, $T(0.5H_{ml}) - T(H_{ml} + \delta h)$, where δh is arbitrarily chosen to be 15 m. The regional map (Fig. A2b) shows that ΔT_E ranges from 0.6°C to ~3°C, which is a conservative estimate compared to 4°C, as chosen by Wyrтки (1981). Because H_{ml} is derived from a variable density criterion, the estimated ΔT_E does not closely reflect H_{ml} particularly in the presence of a barrier layer (Sprintall and Tomczak 1992; de Boyer Montégut et al. 2004).

c. Radiative flux

The HERB product (L'Ecuyer and Stephens 2003, 2007; L'Ecuyer and McGarragh 2010) provides atmospheric radiative flux and heating profiles covering the TRMM-observed region. Instead of directly using broadband spectral measurement, the HERB synthesizes radi-

ative fluxes from cloud and precipitation profiles retrieved from satellite observations together with other parameters, such as air temperature, humidity, and aerosol, using broadband radiative transfer calculations. As such, the HERB dataset provides radiative flux not only at the top of the atmosphere, but at any vertical level. To quantify the radiative effects on the mixed layer heat budget, the downward shortwave and longwave fluxes at the surface, or F_{SW}^\downarrow and F_{LW}^\downarrow , respectively, are taken from the HERB dataset. It has been shown that satellite-based surface radiative flux products, such as the International Satellite Cloud Climatology Project (ISCCP) radiative flux profile data (FD), tend to overestimate surface SW fluxes in tropical regions (Large and Yeager 2009). Based on comparisons against in situ flux measurements at nine ocean sites, L'Ecuyer and McGarragh (2010) estimate that the HERB product may exhibit similar biases of $\sim 18 \text{ W m}^{-2}$. In the current study, the shortwave flux is reduced constantly by 20 W m^{-2} in order to avoid a potential overestimate of the shortwave impact on the ocean heat budget. To test the potential impacts of such an overestimate on the ocean heat budget, separate experiments have been conducted with different SW offsets that indicate that the behavior of the mixed layer heat budget is qualitatively insensitive to errors of this magnitude (not shown). It is further noted that the excess SW heating that may exist in regions with shallow mixed layers can be partially compensated for by tuning both absorptivity and ΔT_E over a realistic range. Finally, L'Ecuyer and McGarragh (2010) demonstrate that, despite any potential biases that may exist in SW fluxes, seasonal and interannual variability in downwelling SW flux estimates are well represented in the HERB product.

The net longwave heat flux at the surface is written as

$$Q_{LW} = F_{LW}^\downarrow + F_{LW}^\uparrow = F_{LW}^\downarrow - \sigma T_s^4 \quad (\text{A14})$$

where $\sigma = 5.67 \times 10^{-8} \text{ W m}^{-2} \text{ K}^{-4}$ is the Stephan-Boltzmann constant. Note that the Q values defined in this study represent heat fluxes (W m^{-2}) according to the oceanographic convention and should not be confused with heating rates (K day^{-1}), which are often denoted by Q in the meteorological contexts. The net shortwave flux absorbed by the ocean mixed layer is

$$Q_{SW} = (1 - \alpha) \Pi F_{SW}^\downarrow, \quad (\text{A15})$$

where α and Π are the ocean surface albedo and the fraction of incoming shortwave energy that is absorbed by the mixed layer. While α , fixed at 0.06 in this work, is relatively uniform across global oceans, Π varies with

different factors including the mixed layer depth and chlorophyll concentration. Ohlmann et al. (1996) estimated Π as 0.80–0.93 for the eastern equatorial Pacific. In the present study, Π is assumed to simply depend on the mixed layer depth as

$$\Pi = 1 - \exp\left(-0.06 \frac{H_{ml}}{[m]}\right), \quad (\text{A16})$$

which yields $\Pi = 0.83$ for $H_{ml} = 30$ m.

REFERENCES

- Benedict, J. J., and D. A. Randall, 2007: Observed characteristics of the MJO relative to maximum rainfall. *J. Atmos. Sci.*, **64**, 2332–2354.
- Bonjean, F., and G. S. E. Lagerloef, 2002: Diagnostic model and analysis of the surface currents in the tropical Pacific Ocean. *J. Phys. Oceanogr.*, **32**, 2938–2954.
- Chou, S.-H., R. M. Atlas, C.-L. Shie, and J. Ardizzone, 1995: Estimates of surface humidity and latent heat fluxes over oceans from SSM/I data. *Mon. Wea. Rev.*, **123**, 2405–2425.
- Curry, J. A., C. A. Clayson, W. B. Rossow, R. Reeder, Y.-C. Zhang, P. J. Webster, G. Liu, and R.-S. Sheu, 1999: High-resolution satellite-derived dataset of the surface fluxes of heat, freshwater, and momentum for the TOGA COARE IOP. *Bull. Amer. Meteor. Soc.*, **80**, 2059–2080.
- Dai, A., 2006: Precipitation characteristics in eighteen coupled climate models. *J. Climate*, **19**, 4605–4630.
- de Boyer Montégut, C., G. Madec, A. Fischer, A. Lazar, and D. Iudicone, 2004: Mixed layer depth over the global ocean: An examination of profile data and a profile-based climatology. *J. Geophys. Res.*, **109**, C12003, doi:10.1029/2004JC002378.
- de Szoeke, S. P., and S.-P. Xie, 2008: The tropical eastern Pacific seasonal cycle: Assessment of errors and mechanisms in IPCC AR4 coupled ocean–atmosphere general circulation models. *J. Climate*, **21**, 2573–2590.
- , Y. Wang, S.-P. Xie, and T. Miyama, 2006: Effect of shallow cumulus convection on the eastern Pacific climate in a coupled model. *Geophys. Res. Lett.*, **33**, L17713, doi:10.1029/2006GL026715.
- Gu, G., R. F. Adler, and A. H. Sobel, 2005: The eastern Pacific ITCZ during the boreal spring. *J. Atmos. Sci.*, **62**, 1157–1174.
- Halpern, D., and C.-W. Hung, 2001: Satellite observations of the southeast Pacific intertropical convergence zone during 1993–1998. *J. Geophys. Res.*, **106**, 28 107–28 112.
- Holton, J. R., J. M. Wallace, and J. A. Young, 1971: On boundary layer dynamics and the ITCZ. *J. Atmos. Sci.*, **28**, 275–280.
- Hubert, L. F., A. F. Krueger, and J. S. Winston, 1969: The double intertropical convergence zone—Fact or fiction? *J. Atmos. Sci.*, **26**, 771–773.
- Jourdan, D., and C. Gautier, 1995: Comparison between global latent heat flux computed from multisensor (SSM/I and AVHRR) and from in situ data. *J. Atmos. Oceanic Technol.*, **12**, 46–72.
- Kemball-Cook, S. R., and B. C. Weare, 2001: The onset of convection in the Madden–Julian oscillation. *J. Climate*, **14**, 780–793.
- Kiladis, G. N., K. H. Straub, and P. T. Haertel, 2005: Zonal and vertical structure of the Madden–Julian oscillation. *J. Atmos. Sci.*, **62**, 2790–2809.
- Kubota, M., N. Iwasaka, S. Kizu, M. Konda, and K. Kutsuwada, 2002: Japanese Ocean Flux Data sets with Use of Remote Sensing Observations (J-OFURO). *J. Oceanogr.*, **58**, 213–225.
- Lagerloef, G. S. E., G. T. Mitchum, R. B. Lukas, and P. P. Niiler, 1999: Tropical Pacific near-surface currents estimated from altimeter, wind, and drifter data. *J. Geophys. Res.*, **104**, 23 313–23 326.
- Large, W. G., and S. G. Yeager, 2009: The global climatology of an interannually varying air–sea flux data set. *Climate Dyn.*, **33**, 341–364.
- , J. C. McWilliams, and S. C. Doney, 1994: Oceanic vertical mixing: A review and a model with a nonlocal boundary layer parameterization. *Rev. Geophys.*, **32**, 363–403.
- L'Ecuyer, T. S., and G. L. Stephens, 2003: The tropical oceanic energy budget from the TRMM perspective. Part I: Algorithm and uncertainties. *J. Climate*, **16**, 1967–1985.
- , and —, 2007: The tropical atmospheric energy budget from the TRMM perspective. Part II: Evaluating GCM representations of the sensitivity of 29 regional energy and water cycles to the 1998–99 ENSO cycle. *J. Climate*, **20**, 4548–4571.
- , and G. McGarragh, 2010: A 10-year climatology of tropical radiative heating and its vertical structure from TRMM observations. *J. Climate*, **23**, 519–541.
- Lietzke, C. E., C. Deser, and T. H. Vonder Haar, 2001: Evolutionary structure of the eastern Pacific double ITCZ based on satellite moisture profile retrievals. *J. Climate*, **14**, 743–751.
- Lin, X., and R. H. Johnson, 1996: Kinematic and thermodynamic characteristics of the flow over the western Pacific warm pool during TOGA COARE. *J. Atmos. Sci.*, **53**, 695–715.
- Liu, W. T., and X. Xie, 2002: Double intertropical convergence zones—A new look using scatterometer. *Geophys. Res. Lett.*, **29**, 2072, doi:10.1029/2002GL015431.
- Locarnini, R. A., A. V. Mishonov, J. I. Antonov, T. P. Boyer, and H. E. Garcia, 2006: *Temperature*. Vol. 1, *World Ocean Atlas 2005*, NOAA Atlas NESDIS 61, 182 pp.
- Masunaga, H., T. S. L'Ecuyer, and C. D. Kummerow, 2005: Variability in the characteristics of precipitation systems in the tropical Pacific. Part I: Spatial structure. *J. Climate*, **18**, 823–840.
- , —, and —, 2006: The Madden–Julian oscillation recorded in early observations from the Tropical Rainfall Measuring Mission (TRMM). *J. Atmos. Sci.*, **63**, 2777–2794.
- Mechoso, C. R., and Coauthors, 1995: The seasonal cycle over the tropical Pacific in coupled ocean–atmosphere general circulation models. *Mon. Wea. Rev.*, **123**, 2825–2838.
- Mitchell, T. P., and J. M. Wallace, 1992: The annual cycle in equatorial convection and sea surface temperature. *J. Climate*, **5**, 1140–1156.
- Ohlmann, J. C., D. A. Siegel, and C. Gautier, 1996: Ocean mixed layer radiant heating and solar penetration: A global analysis. *J. Climate*, **9**, 2265–2280.
- Philander, S. G. H., D. Gu, D. Halpern, G. Lambert, N.-C. Lau, T. Li, and R. C. Pacanowski, 1996: Why the ITCZ is mostly north of the equator. *J. Climate*, **9**, 2958–2972.
- Pike, A. C., 1971: Intertropical convergence zone studied with an interacting atmosphere and ocean model. *Mon. Wea. Rev.*, **99**, 469–477.
- Schulz, J., J. Meywerk, S. Ewald, and P. Schlüssel, 1997: Evaluation of satellite-derived latent heat fluxes. *J. Climate*, **10**, 2782–2795.
- Sprintall, J., and M. Tomczak, 1992: Evidence of the barrier layer in the surface layer of the tropics. *J. Geophys. Res.*, **97**, 7305–7316.

- Waliser, D. E., and R. C. J. Somerville, 1994: Preferred latitudes of the intertropical convergence zone. *J. Atmos. Sci.*, **51**, 1619–1639.
- Wang, B., and Y. Wang, 1999: Dynamics of the ITCZ–equatorial cold tongue complex and causes of the latitudinal climate asymmetry. *J. Climate*, **12**, 1830–1847.
- Wyrtki, K., 1981: An estimate of equatorial upwelling in the Pacific. *J. Phys. Oceanogr.*, **11**, 1205–1214.
- Xie, S.-P., 1994: Oceanic response to the wind forcing associated with the intertropical convergence zone in the Northern Hemisphere. *J. Geophys. Res.*, **99**, 20 393–20 402.
- , and S. G. H. Philander, 1994: A coupled ocean–atmosphere model of relevance to the ITCZ in the eastern Pacific. *Tellus*, **46**, 340–350.
- , and Coauthors, 2007: A regional ocean–atmosphere model for eastern Pacific climate: Toward reducing tropical biases. *J. Climate*, **20**, 1504–1522.
- Zhang, C., 1996: Atmospheric intraseasonal variability at the surface in the tropical western Pacific Ocean. *J. Atmos. Sci.*, **53**, 739–758.
- , 2001: Double ITCZs. *J. Geophys. Res.*, **106**, 11 785–11 792.